Title	Study of the cation distributions in Eu doped Sr2Y8(SiO4)6O2 by X-ray diffraction and photoluminescent spectra
Author(s)	Shen, Yiqiang; Chen, Rui; Xiao, Fen; Sun, Handong; Tok, Alfred Iing Yoong; Dong, Zhili
Citation	Shen, Y., Chen, R., Xiao, F., Sun, H., Tok, A., & Dong, Z. (2010). Study of the cation distributions in Eu doped Sr2Y8(SiO4)6O2 by X-ray diffraction and photoluminescent spectra. Journal of Solid State Chemistry, 183(12), 3093-3099.
Date	2010
URL	http://hdl.handle.net/10220/8827
Rights	© 2010 Elsevier Inc. This is the author created version of a work that has been peer reviewed and accepted for publication by Journal of Solid State Chemistry, Elsevier Inc. It incorporates referee's comments but changes resulting from the publishing process, such as copyediting, structural formatting, may not be reflected in this document. The published version is available at: [DOI: http://dx.doi.org/10.1016/j.jssc.2010.10.025].

Study of the cation distributions in Eu doped $Sr_2Y_8(SiO_4)_6O_2$ by X-ray diffraction and photoluminescent spectra

Yiqiang Shen[a], Rui Chen[b], Fen Xiao[b], Handong Sun[b], Alfred Tok[a], Zhili Dong[a,*]

[a] *School of Materials Science and Engineering, Nanyang Technological University, Block N4.1 Level 1, 50 Nanyang Avenue, Singapore 639798, Singapore*

[b] *Division of Physics and Applied Physics, School of Physical and Mathematical Sciences, Nanyang Technological University, Singapore 637371, Singapore*

[*] *Corresponding author. Fax: +65 67909081.*

E-mail addresses: SHEN0061@ntu.edu.sg (Y. Shen), CHEN0529@ntu.edu.sg (R.Chen), PG36812735@ntu.edu.sg (F. Xiao), HDSUN@ntu.edu.sg (H. Sun), MIYTOK@ntu.edu.sg (A. Tok), ZLDONG@ntu.edu.sg (Z. Dong).

Abstract

The crystal structure and photoluminescent properties of europium doped silicate $Sr_2Y_8(SiO_4)_6O_2:Eu^{3+}$ are reported. The $Sr_2Y_{8-x}Eu_x(SiO_4)_6O_2$ compounds have typical apatite crystal structures with the $P6_3/m$ space group. The distributions of Eu^{3+} between the two crystallographic sites 4*f* and 6*h* in the apatite structure are investigated by the powder X-ray diffraction and Rietveld refinement. Results show that Eu^{3+} ions only occupy the 4*f* sites when the Eu doping concentration is low ($x = 0$–0.5 in $Sr_2Y_{8-x}Eu_x(SiO_4)_6O_2$). However, in higher concentrations, Eu^{3+} ions begin to enter the *6h* sites as well. The distributions of the Eu^{3+} are also reflected in photoluminescent spectra. The CIE coordinates for $Sr_2Y_6Eu_2(SiO_4)_6O_2$ are (0.63, 0.37), which is close to the pure red color.

1. Introduction

Apatite-type materials are an interesting family in the crystallographic studies due to the existence of two distinct cationic sites and their tolerance to incorporate different ions [1–4]. Most apatite-type materials belong to the space group $P6_3/m$ though some variants adopt the space groups with lower symmetries (e.g. $P6_3$ and $P2_1/m$) [5]. The general formula is $A^{\mathrm{I}}_4A^{\mathrm{II}}_6(BO_4)_6X_2$, where A^{I} and A^{II} positions with Wyckoff symbols 4*f* and 6*h*, respectively, can accommodate alkali, alkaline-earth or rare-earth atoms. The *B* tetrahedral site is occupied by phosphorous, vanadium, silicon, boron or germanium, and the *X* anion site is for halogen, hydroxyl or oxygen. The characterizations of the crystal structures of various apatite-type materials have provided fundamental understandings for their applications in the areas of bone replacement [6], catalysis [7] and environmental remediation [8]. More recently new applications

of apatite-type materials have emerged. For example, rare-earth doped silicate oxy-apatites could be used in optical devices such as laser media [9–11] and scintillators [12] due to their good thermal and chemical stabilities [13]. The rare earth dopants are known as activators which provide the desired energy levels for electronic transitions. The silicate oxy-apatites not only act as the host materials to support and dilute the activators but also to influence the electronic structures of the dopants. Since the two types of cationic sites, 4*f* and 6*h*, that host the rare earth elements have different chemical environments, different electronic structures for rare earth cations at the two sites are expected. Therefore, it is pre-requisite to understand the distributions of the rare earth elements between these two cationic sites for further optical property study.

Among the rare earth cations, Eu^{3+} is not only a widely used red light emitter for optical devices [14] but also a probe for the local crystal structures [15]. The electronic transitions within the 4*f* shell of Eu^{3+} cation are sensitive to the local symmetries as the magnetic dipole transition $^5D_0 \rightarrow {}^7F_1$ of Eu^{3+} and the electric dipole transition $^5D_0 \rightarrow {}^7F_2$ are sensitive to the inverse center. In addition, the $^5D_0 \rightarrow {}^7F_0$ transition is strongly affected by the linear crystal field term [16,17]. In order to avoid the confusion with '4*f*' used as the crystallographic site, the term of 4*f* standing for the electron shell of Eu^{3+} is written in italic. By studying these characteristic transitions in the photoluminescent spectra, more information about crystal structures can be obtained [18–20]. However, most of these studies focused on the photoluminescent spectra analysis with less attention to X-ray diffraction (XRD) and the Rietveld refinement structure determination, although the later are powerful tool for crystal structure analysis.

In the present study, apatite-type $Sr_2Y_8(SiO_4)_6O_2$ and Eu^{3+} were chosen as the host and dopant, respectively. $Sr_2Y_8(SiO_4)_6O_2$ apatite has been used as host materials in the ultrafast laser system [9–11], and it possesses $P6_3/m$ symmetry with Sr^{2+} and Y^{3+} randomly distributed in the 4*f* sites and Y^{3+} fully occupied the 6*h* sites [21]. After sol–gel synthesis, the distribution of Eu^{3+} dopant between the two cationic sites in $Sr_2Y_8(SiO_4)_6O_2$ apatite was analyzed through the combination of X-ray diffraction, the Rietveld refinement and the photoluminescent spectra.

2. Materials and methods

Silicate oxy-apatites $Sr_2Y_{8-x}Eu_x(SiO_4)_6O_2$ (x=0.05–5) were prepared by sol–gel method. For each composition, 0.002 mol powders were produced. First, stoichiometric amount of strontium nitrate $Sr(NO_3)_3$ (Fluka, >99.9%), hexahydrate yttrium nitrate $Y(NO_3)_3 \cdot H_2O$ (Sigma-Aldrich, >99.9%) and europium acetate $Eu(CH_3COO)_3$ (Sigma-Aldrich, >99.9%) were dissolved in deionized water in one beaker. And then 2.66 ml tetraethoxysilane $Si(OC_2H_5)_4$ (TEOS, Sigma-Aldrich, >99.99%) was mixed with 6 ml absolute enthonal and 6 ml acetic acid in another beaker. When the transparent solutions in both beakers were obtained, the two solutions were mixed together and refluxed at 110 °C until homogeneous gel was formed. The viscous gel was dried at 80 °C for 12 h followed by a heating at 700 °C for 4 h in order to remove the residual organic species. After that, the products were fully ground and heat treated at 1400 °C for 6 h in a muffle

furnace, until the apatite powder materials were obtained.

The phase compositions of the as-synthesized samples were studied by X-ray diffraction. The data were collected using the Shimadzu 6000 X-ray diffractometer with Cu$K\alpha$ radiation. The machine was operated at 40 kV and 40 mA with a 2θ step size of 0.02° and a scan rate of 2°/min. Furthermore, Rietveld refinement was carried out using TOPAS (Version 3.0. Bruker AXS, Karlsruhe, Germany). The crystal structure of $Sr_2Y_8(SiO_4)_6O_2$ had been studied previously [21] and the structure model of it was used in the present study. The parameters were refined in the following sequence: background by using Chebychev function, cell parameters, crystal size, atom positions, global thermal parameters, and site occupancies. Since the Eu^{3+} just substitutes the Y^{3+}, the site occupancy of Sr^{2+} at 4*f* is fixed as 0.5 according to the last study. Assuming that *x* is the total amount of Eu doped into $Sr_2Y_{8-x}Eu_x(SiO_4)_6O_2$ and the site occupancy of Eu^{3+} at the 6*h* site is *n*, the site occupancy of Y^{3+} at 6*h* is $1-n$ and that of Eu^{3+} and Y^{3+} at the 4*f* site is $(x-6n)/4$ and $(2-x+6n)/4$, respectively. These parameters were input into the refinement software during refining the site occupancies of Eu^{3+} and Y^{3+}.

The high resolution transmission electron microscopy (HRTEM) images were collected using a JEOL JEM-2100F microscope (Cs=0.5 mm, accelerating voltage=200 kV).

The conventional photoluminescent (PL) and photoluminescent excitation (PLE) measurements were carried out using a Shimadzu RF-5301PC spectrophotometer. In order to distinguish the peaks that are close to each other, subsequent high resolution PL and PLE measurements were conducted. In these measurements, a 450 W Xenon lamp combined with a 0.3 m grating monochromator was used as the excitation source. The signal was dispersed by a 0.75 m monochromator combined with suitable filters, and detected by a photomultiplier using the standard lock-in amplifier technique. The widths of the entrance and exit slits of the monochromator were set at 20 μm, with which the resolution of spectra near the wavelength of 578 nm is ~0.05 nm.

3. Results and discussion

3.1. Characterization of the crystal structures of $Sr_2Y_{8-x}Eu_x(SiO_4)_6O_2$

XRD results of all the compounds $Sr_2Y_{8-x}Eu_x(SiO_4)_6O_2$($x$=0.05,0.1, 0.5, 1, 2, 5) indicated that pure apatite phases were obtained after sol–gel synthesis followed by the heat treatment. The Rietveld refinement showed low *R* values (see Table 1) for all the XRD patterns from the above compounds with the hexagonal space group $P6_3/m$, indicating the reliability of the refinement results. The XRD and Rietveld refined patterns of $Sr_2Y_6Eu_2(SiO_4)_6O_2$ are shown in Fig. 1. The small black circles are experimental X-ray diffraction data, the red pattern is calculated from the refinement and the gray pattern is the difference between the experimental data and the calculated ones. All the experimental peaks are well fitted by the refinement, indicating that all of those

peaks are Bragg reflections from the $Sr_2Y_6Eu_2(SiO_4)_6O_2$ structure and the purity of the as-synthesized $Sr_2Y_6Eu_2(SiO_4)_6O_2$ is high. Since there are too many Bragg reflections of the apatite phase in the XRD pattern, only eight of them with the highest intensities are indexed. The XRD patterns of $Sr_2Y_{8-x}Eu_x(SiO_4)_6O_2$ (x = 0.05, 0.1, 0.5, 1, 2, 5) are shown in Fig. 2a and their identical shapes demonstrates the high purities of all these samples. The small deviations between the present refinement data and the previous study [21] may be due to different synthesis methods. Fig. 2b shows that the lattice parameters a and c expand as the Eu doping concentration increases, due to the substitutions of larger sized Eu^{3+} ($r_{Eu^{3+}}$ = 0.95 Å when CN= 6) for Y^{3+} ($r_{Y^{3+}}$ = 0.9 Å when CN= 6). Based on the crystallographic data from one of the compound series, $Sr_2Y_6Eu_2(SiO_4)_6O_2$, the atomic positions are listed (Table 2) and the characteristic polyhedral network is displayed in Fig. 3. This network consists of three different types of polyhedra, 4*f*—O, 6*h*—O and Si—O. Although most of the oxygen atoms can be included into Si—O polyhedra, the O(4) atoms, or free oxygen, cannot be linked to any of them. Among the three types of polyhedra, the 4*f*—O is formed by the cations at the 4*f* site and nine surrounding oxygen anions. The nine oxygen anions (3 × O(1), 3 × O(2) and 3 × O(3)) belong to two different Wyckoff sites, and polyhedron exhibits a tricapped trigonal-prismatic geometry. The bond lengths of 4f—O(1), 4f—O(2) and 4f—O(3) are 2.325, 2.511 and 2.811 Å, respectively. The cation at the 6*h* site and seven coordinated oxygen anions form an irregular polyhedron with pentagonal bipyramidal geometry. The bond lengths between the 6*h* site and these oxygen atoms range from 2.206 to 2.658 Å (Table 3). Among those oxygen atoms around 6*h*, the free oxygen O(4) is bonded to the cation at the 6*h* site in a short distance (2.206 Å). Based on the bond length data related to O(4) and cations at the 6*h* sites, the oxygen atom is underbonded as its calculated valence is only 1.79 [22].

Moreover, the distributions of the Eu^{3+} between the 4*f* and 6*h* sites at different doping concentrations were also revealed by the refinement. The refinement result showed that most of the Eu^{3+} entered the 4*f* site when the Eu doping concentration was low (x = 0–0.05). This phenomenon is in line with Blasse's theory of the site occupancy [23]. Since the 6*h* site links to one underbonded free oxygen, the cations with smaller radius and higher charge prefer entering this position to compensate the charge. The radius of Eu^{3+} is larger than that of Y^{3+}, therefore Eu^{3+} cations prefer the 4*f* sites. Although the site preference still maintains, the Eu^{3+} begins to occupy the 6*h* site in higher Eu doping concentration ($x \geq 0.5$). Some discrepancy from linearity in the relationship between Eu concentration and lattice parameters occurs around x = 0.5–1, which may be attributed to the Eu^{3+} occupancy in the 6*h* site. Not only would the Eu^{3+} distribution evolve with the changes of the Eu^{3+} doping concentrations, so would the polyhedral network. The average bond lengths in 4*f*−O and 6*h*−O polyhedra for samples x =1, 2, 5 are listed in Table 3. Although the average bond length al one cannot represent the polyhedral network completely, it would demonstrate some trend in the evolution of the crystal structures. The average bond lengths in 6*h*−O polyhedra expand from 2.419 to 2.430 Å with the increase of the Eu doping concentration. In higher Eu doping concentration, large amount of Eu^{3+} substitute the relatively smaller Y^{3+} at the 6*h* site, which enlarges the polyhedral volumes and results in longer average bond lengths. In the polyhedral networks presented in Fig. 3, six columns of 6*h* atoms (z =1/4 and

3/4) surrounding the column of free oxygen (z = 1/4 and 3/4) are close and there are no other atom columns in-between. For the cations at the 6*h* sites, two main kinds of Coulomb interactions exist, one is the repulsive force between these neighboring cationic columns at the 6*h* sites, and the other is the attractive force between the 6*h* cation and the free oxygen. When the larger-sized Eu^{3+} occupy the 6*h* sites, the repulsive force would slightly expand the six 6*h* columns surrounding the free oxygen column, leading to the elongation of average bond length. Interestingly, the average bond length in 4*f*- O polyhedra is shortened (from 2.579 to 2.512 Å) with the increase of the Eu doping concentration. A possible explanation is that the columns of 4*f* atoms are disconnected by Si − O polyhedra and the repulsive interaction between the 4*f* atoms is weakened. Furthermore, the Si - O polyhedra can twist the 4*f*- O polyhedra, resulting in smaller average bond length.

In order to further analyze the crystal structure, a high resolution transmission electron microscopy image of $Sr_2Y_6Eu_2(SiO_4)_6O_2$ and the corresponding FFT pattern along the *c*-axis are shown in Fig. 4. The *d*-spacing of $(10\bar{1}0)$ plane is about 8.1 Å. According to the crystallographic features, the *d*-spacing value of $(10\bar{1}0)$ also can be derived from the lattice parameters obtained from the XRD refinement (Table 1) as

$$d_{(10\bar{1}0)} = a\cos 30^\circ = 9.3911\frac{\sqrt{3}}{2}\,\text{Å} = 8.1329\,\text{Å} \approx 8.1\,\text{Å}$$

The consistency between the XRD refinement and the HRTEM results substantiates the analysis above.

3.2. Photoluminescence properties

The PLE spectra of $Sr_2Y_{8-x}Eu_x(SiO_4)_6O_2$ (x = 0.05, 0.1, 0.5, 1, 2, 2.5, 5) monitored at 613 nm are shown in Fig. 5. The broad band in the range of 250-300 nm corresponds to the $Eu^{3+}-O^{2-}$ charge transfer band (CTB), which is allowed by the selection rules. The sharp excitation peaks between 350 and 450 nm are attributed to the intra-4*f* transitions from the Eu^{3+} ground state $^7F_0$. The 4*f* electrons in Eu^{3+} are well shielded by the 5*d* electrons, so the different environments have little effect on the 4*f* energy levels. Therefore, the intra-4*f* transitions for both the 4*f* and 6*h* sites appear at the same position in PLE. The intensities of the intra-4*f* transitions increase rapidly with the increase of the Eu doping concentration when $x \leq 2$, which can be ascribed to the following two reasons. The first reason is that no matter whether Eu^{3+} occupies the 4*f* site or 6*h* site, every individual Eu^{3+} contributes to the overall intensities of the intra-4*f* transitions and also the CTB. Therefore, the more the Eu^{3+} doped into the structure, the higher the overall intensities of the intra-4*f* transitions in PLE as long as no concentration quenching occurs, which is also why the intensities of CTB increase with the increase of the Eu doping concentration when $x \leq 2$. However, it is obvious that the increase of intensities for intra-4*f* transitions is more rapid than that of the CTB. It could be ascribed to the second reason which is related to the relaxation of the intra-4*f* transitions at the 6*h* sites. The intra-4*f* transitions are forbidden by the parity selection

rule, but this selection rule could relax when uneven components of the crystal field exist because the uneven components can mix the opposite parity 5*d* wave functions into the 4*f* wave functions [24,25]. As mentioned above, the cations at the 6*h* site are bonded with O(4) free oxygen, which would exert a linear crystal field to the 6*h* site [23]. However, there is no such kind of free oxygen bonded with the cations at the 4*f* site. Thus, the intra-4*f* transitions of Eu^{3+} in the 6*h* sites are more probable and possess higher intensities than in the 4*f* sites. According to the analysis of the site occupancies, the amount of the Eu^{3+} in the 6*h* site increases when the total doping concentration increases. So the intra-4*f* transitions are intensified by increasing the Eu doping concentration and the highest intensity of the $^7F_0-^5L_6$ transition appears at $x = 2$. Moreover, the intensities of the intra-4*f* transitions in the PLE decrease when $x > 2$ due to the concentration quenching effect.

Another feature of the photoluminescence excitation (PLE) spectra is the position of the CTB. The CTB is located around 273 nm at lower doping concentration, and it shifts to longer wavelength and reaches 289 nm in $Sr_2Y_3Eu_5(SiO_4)_6O_2$. This shifting is caused by the variation of the Eu^{3+} occupancies between the 4*f* and 6*h* sites. In higher doping concentration, Eu^{3+} would accumulate at the 6*h* sites, which are closely bonded with the free oxygen. Compared to other pairs of Eu^{3+}–O^{2-} bonds in the structure, this closely bonded pair Eu–O(4) leads to more overlapping between the cation and anion orbitals, which further reduces the the energy required to transfer one electron from the O^{2-} to Eu^{3+} [26].

Since the $^7F_0$-$^5L_6$ transition at 393 nm is pronounced, the photoluminescent (PL) properties of this series of apatites excited at 393 nm was further studied (Fig. 6). Under this excitation, the phosphors exhibit red emission. The emission spectra consist of several sharp peaks which corresponds to the intra-4*f* transitions $^5D_0\rightarrow{}^7F_{0,1,2,3,4}$ (Fig. 6a). No emission from higher levels of $^5D_1$ or $^5D_2$ was observed, because the electrons at higher levels would nonradiatively decay to the level $^5D_0$ by the multiphonon relaxation process caused by the presence of the host lattice with relatively high vibration frequency ($\upsilon_{SiO4} = 930cm^{-1}$). The emission peak at 613 nm belongs to the forced electric-dipole transition $^5D_0\rightarrow{}^7F_2$. The intensity of this emission is much higher than that of the magnetic-dipole transition $^5D_0\rightarrow{}^7F_1$, which supports the conclusion of the XRD analysis that no inversion center exists in the structure [27]. Consistently with the PLE spectra, the highest intensity of the $^5D_0\rightarrow{}^7F_2$ transition occurs when x=2 in the $Sr_2Y_{8-x}Eu_x(SiO_4)_6O_2$ series (Fig. 6b). Further increase in doping concentration reduces the intensities due to the concentration quenching effect. Statistically, the distances between the activators become shorter with higher doping concentration. Once this distance is shorter than a critical value, the energy is more likely to transfer from one activator to another and eventually reach the quenching sites, rather than being released from individual activators in the form of light emission. Therefore, the intensities of the emission become lower. This critical distance *R* can be estimated by the following equation [28,29]:

$$R \approx 2\left(\frac{3V}{4\pi x N}\right)^{1/3} \quad (1)$$

where x is the critical concentration, V is the volume of the unit cell and N is the number of the host cationic sites in the unit cell. In the current case, V is 526.4 $Å^3$, N is 8 and x is about 2, therefore the critical distance is about 4 Å. When the distance between the Eu^{3+} is less than 4 Å, a certain wave function overlap between the Eu^{3+} occurs and the energy transfers from one site to another by the exchange interaction [30]. In fact, the nearest distances of 4*f*–4*f*, 4*f*–6*h* and 6*h*–6*h* are about 3.5, 4.0 and 4.1 Å, respectively, based on the Rietveld refinement results, which is comparable to the value of critical distance. Eu^{3+} cations become neighbors in high Eu^{3+} concentration, e.g. $Sr_2Y_3Eu_5(SiO_4)_6O_2$, and the energy migration occurs, resulting in the concentration quenching effect.

The energy level of ^7F_J ($J > 0$) would split with the influence of the surrounding ions, resulted in the appearance of several peaks for any $^5D_0 \rightarrow {}^7F_J$ ($J > 0$) transition in the emission spectra. However, no energy split occurs for the energy level with J=0. Therefore, the $^5D_0 \rightarrow {}^7F_0$ transition of Eu^{3+} has a single peak for each site in the emission spectra, and the number of the $^5D_0 \rightarrow {}^7F_0$ transition peaks denotes the number of the cationic sites the Eu^{3+} occupied. From the high resolution PL spectra of the $^5D_0 \rightarrow {}^7F_0$ transition of $Sr_2Y_6Eu_2(SiO_4)_6O_2$, which is shown in Fig. 7, the two peaks of $^5D_0 \rightarrow {}^7F_0$ transition appeared, suggesting that Eu^{3+} entered both the 6*h* and 4*f* sites. After Gaussian fitting, the positions of two peaks have been identified at 577.5 nm (α) and 578.5 nm (β). High resolution PLE spectra were monitored the emission wavelength at 577.5 and 578.5 nm and are shown in Fig. 7b. The position of the CTB corresponding to the β peak is at 292.9 nm, but the one corresponding to α peak has shifted to 297.5 nm. Since the free oxygen is closely bonded to the 6*h* site and their orbitals are mixed, the CTB of the activators at the 6h sites would appear at lower energy and longer wavelength. So the α peak corresponds to the Eu^{3+} at the 6*h* sites and the β peak belongs to the Eu^{3+} at the 4*f* sites. The samples with x = 5 was compared with the one with x = 2. No obvious difference was observed. Only the α peak corresponding to the 6*h* site at shorter wavelength become slightly higher as compared to the β peak in the sample x = 5 as shown in Fig. 7c. The peak intensities do not vary as much with the Eu doping concentrations as the site occupancies. The most reasonable explanation is that part of the energy in Eu^{3+} at the 6*h* sites is transferred to those at the 4*f* sites. Further studies about this energy transfer behavior between the 6*h* and 4*f* sites are undergoing.

Moreover, the CIE coordinates are (0.63, 0.37) for $Sr_2Y_6Eu_2(SiO_4)_6O_2$, which is close to the National Television System Committee (NTSC) standard red (0.67, 0.33) as the pure red color. The effective excitation of the $^7F_0 \rightarrow {}^5L_6$ transition and the nearly pure red color make sure that the Eu: $Sr_2Y_8(SiO_4)_6O_2$ will be a promising phosphor for white LED applications.

4. Conclusion

The $Sr_2Y_{8-x}Eu_x(SiO_4)_6O_2$ compounds have typical apatite crystal structures with $P6_3/m$ symmetries, and two cationic sites 4*f* and 6*h*. The photoluminescent spectra analysis and the Rietveld refinement results indicate that the Eu^{3+} ions enter the 4*f* sites at lower doping concentrations, and occupy both the 4*f* and 6*h* sites at higher doping concentrations. When excited by near-UV light with a wavelength of 393 nm, the series of compounds emit red light with a wavelength of 613 nm. The CIE coordinates for $Sr_2Y_6Eu_2(SiO_4)_6O_2$ are (0.63, 0.37) which is close to the pure red color.

Acknowledgments

We are thankful for financial support from the NTU Research Scholarship and NTU AcRF grant (RG11/04).

Appendix A. Supplementary material

Supplementary data associated with this article can be found in the online version at doi:10.1016/j.jssc.2010.10.025.

References

[1] M.I. Kay, R.A. Young, A.S. Posner, Nature 204 (1964) 1050–1052.
[2] Z.L. Dong, T.J. White, B. Wei, K. Laursen, J. Am. Ceram. Soc. 85 (2002) 2515–2522.
[3] J.Y. Kim, Z.L. Dong, T.J. White, J. Am. Ceram. Soc. 88 (2005) 1253–1260.
[4] P.H.J. Mercier, Y. Le Page, P.S. Whitfield, L.D. Mitchell, J. Appl. Crystallogr. 39 (2006) 369–375.
[5] T.J. White, Z.L. Dong, Acta Crystallogr. B: Struct. Sci. 59 (2003) 1–16.
[6] W. Suchanek, M. Yoshimura, J. Mater. Res. 13 (1998) 94–117.
[7] B.M. Choudary, C. Sridhar, M.L. Kantam, G.T. Venkanna, B. Sreedhar, J. Am. Ceram. Soc. 127 (2005) 9948–9949.
[8] X.B. Chen, J.V. Wright, J.L. Conca, L.M. Peurrung, Environ. Sci. Technol. 31 (1997) 624–631.
[9] F. Druon, F. Balembois, P. Georges, Opt. Express 12 (2004) 5005–5012.
[10] F. Druon, S. Chenais, F. Raybaut, Opt. Lett. 27 (2002) 1914–1916.
[11] F. Druon, P. Georges, Opt. Express 12 (2004) 3383–3396.
[12] B. Francois, M. Navizet, J. Rebreyend, C. Won, U.S. Patent no. 4988882, 1991.
[13] J.C. Souriau, R. Romero, C. Borel, C. Wyon, C. Li, R. Moncorge, Appl. Phys. Lett. 64 (1994) 1189–1191.
[14] W.T. Carnall, P.R. Fields, K. Rajnak, J. Chem. Phys. 49 (1968) 4450–4455.
[15] N. Lakshminarasimhan, U.V. Varadaraju, J. Solid State Chem. 177 (2004) 3536–3544.
[16] W.C. Nieuwpoo, G. Blasse, Solid State Commun. 4 (1966) 227–229.
[17] G. Blasse, A. Bril, W.C. Nieuwpoo, J. Phys. Chem. Solids 27 (1966) 1587–1592.
[18] R. Jagannathan, M. Kottaisamy, J. Phys.: Condens. Matter 7 (1995) 8453–8466.
[19] Y.C. Li, Y.H. Chang, B.S. Tsai, Y.C. Chen, Y.F. Lin, J. Alloys Compd. 416 (2006) 199-205.
[20] J. Lin, Q. Su, Mater. Chem. Phys. 38 (1994) 98–101.
[21] Y.Q. Shen, A. Tok, D.Y. Tang, Z.L. Dong, J. Am. Ceram. Soc. 93 (2010) 1176–1182.
[22] I.D. Brown, D. Altermatt, Acta Crystallogr. B: Struct. Sci. 41 (1985) 244–247.
[23] G. Blasse, J. Solid State Chem. 14 (1975) 181–184.
[24] B.R. Judd, Phys. Rev. 127 (1962) 750–761.
[25] G.S. Ofelt, J. Chem. Phys. 37 (1962) 511–520.
[26] G. Blasse, J. Chem. Phys. 45 (1966) 2356–2360.
[27] G. Blasse, B.C. Grabmaier, Luminescent Materials, Springer-Verlag, Berlin, 1994.
[28] G. Blasse, Philips Res. Rep. 24 (1969) 131.
[29] X.M. Liu, C.K. Lin, J. Lin, Appl. Phys. Lett. 90 (2007) 081904.
[30] G. Blasse, J. Chem. Phys. 46 (1967) 2583–2585.

List of Tables

Table 1

	a (Å)	c (Å)	R_{Bragg} (%) [a]	R_p (%) [b]	R_{wp} (%) [c]	Eu at 4*f*	Eu at 6*h*	V (Å^3)
X=0.05	9.3804(9)	6.8681(1)	1.204	3.79	4.78	0.0125	0	523.382(5)
X=0.1	9.3808(7)	6.8711(9)	2.047	6.36	9.27	0.0250	0	523.658(1)
X=0.5	9.3854(2)	6.8800(3)	1.781	6.51	8.97	0.1096	0.0103	524.837(4)
X=1	9.3884(9)	6.8820(1)	1.033	3.31	4.29	0.1491	0.0673	525.326(4)
X=2	9.3911(2)	6.8922(1)	2.512	3.52	4.70	0.2758	0.1501	526.422(6)
X=5	9.3941(8)	6.9146(2)	2.266	4.07	5.16	0.5	0.5	528.469(2)

[a]

$$R_{Bragg} = \frac{\sum |I_{k,obs} - I_{k,calc}|}{\sum I_{k,obs}}.$$

[b]

$$R_{wp} = \sqrt{\frac{\sum w_m (Y_{m,obs} - Y_{m,calc})^2}{\sum w_m Y_{m,obs}{}^2}}.$$

[c]

$$R_p = \sqrt{\frac{\sum w_m |Y_{m,obs} - Y_{m,calc}|}{\sum Y_{m,obs}}}.$$

Where $I_{k,obs}$ and $I_{k,calc}$ are the observed and calculated intensities of the kth reflection, respectively; w_m is the reciprocal of the variance for each observation; $Y_{m,obs}$ and $Y_{m,calc}$ are the observed and calculated data, respectively, at data point m.

Atom	Wyckoff symbol	x/a	y/b	z/c	B_{eq} (Å^2)[a]
Y/Eu	6*h*	0.23131	0.99287	1/4	1.033
Y/Sr/Eu	4*f*	1/3	2/3	0.00412	1.842
Si	6*h*	0.39659	0.37084	1/4	0.847
O1	6*h*	0.31448	0.48850	1/4	0.201
O2	6*h*	0.58600	0.47145	1/4	0.397
O3	12*i*	0.34102	0.25627	0.06738	1.21
O4	2*a*	0	0	1/4	1.519

[a] The isotropic temperature factor $B_{eq}=U_{iso}\times 8\times \pi^2$.

Table 2

Sites	Bond	$X=1$	$X=2$	$X=5$
4*f*	$3\times$ 4*f*–O1	2.421(2)	2.325(9)	2.354(7)
	$3\times$ 4*f*–O2	2.469(7)	2.511(1)	2.413(5)
	$3\times$ 4*f*–O3	2.848(1)	2.811(8)	2.769(6)
	Average	2.579(3)	2.549(6)	2.512(6)
6*h*	6*h*–O4	2.199(4)	2.206(2)	2.217(3)
	$2\times$ 6*h*–O3	2.389(8)	2.354(7)	2.343(5)
	6*h*–O2	2.443(6)	2.430(9)	2.418(8)
	$2\times$ 6*h*–O3	2.475(8)	2.493(5)	2.502(6)
	6*h*–O1	2.565(9)	2.658(7)	2.686(1)
	Average	2.419(7)	2.427(5)	2.430(5)

Table 3

List of Figures

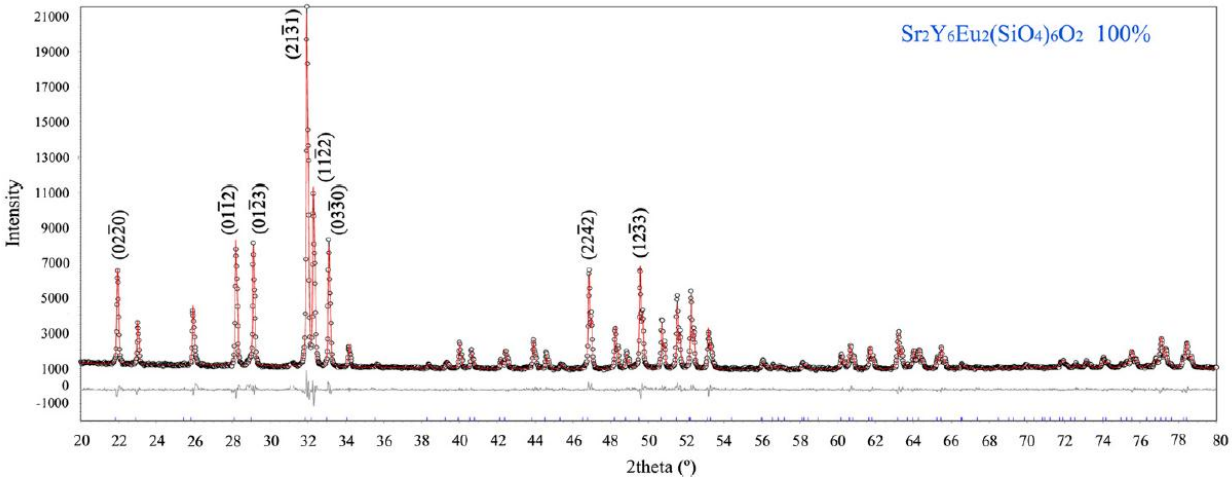
Sr2Y6Eu2(SiO4)6O2 100%
Intensity
2theta (°)
(02$\bar{2}$0)
(01$\bar{1}$2)
(01$\bar{2}$3)
(21$\bar{3}$1)
(11$\bar{2}$2)
(03$\bar{3}$0)
(22$\bar{4}$2)
(12$\bar{3}$3)

Fig. 1

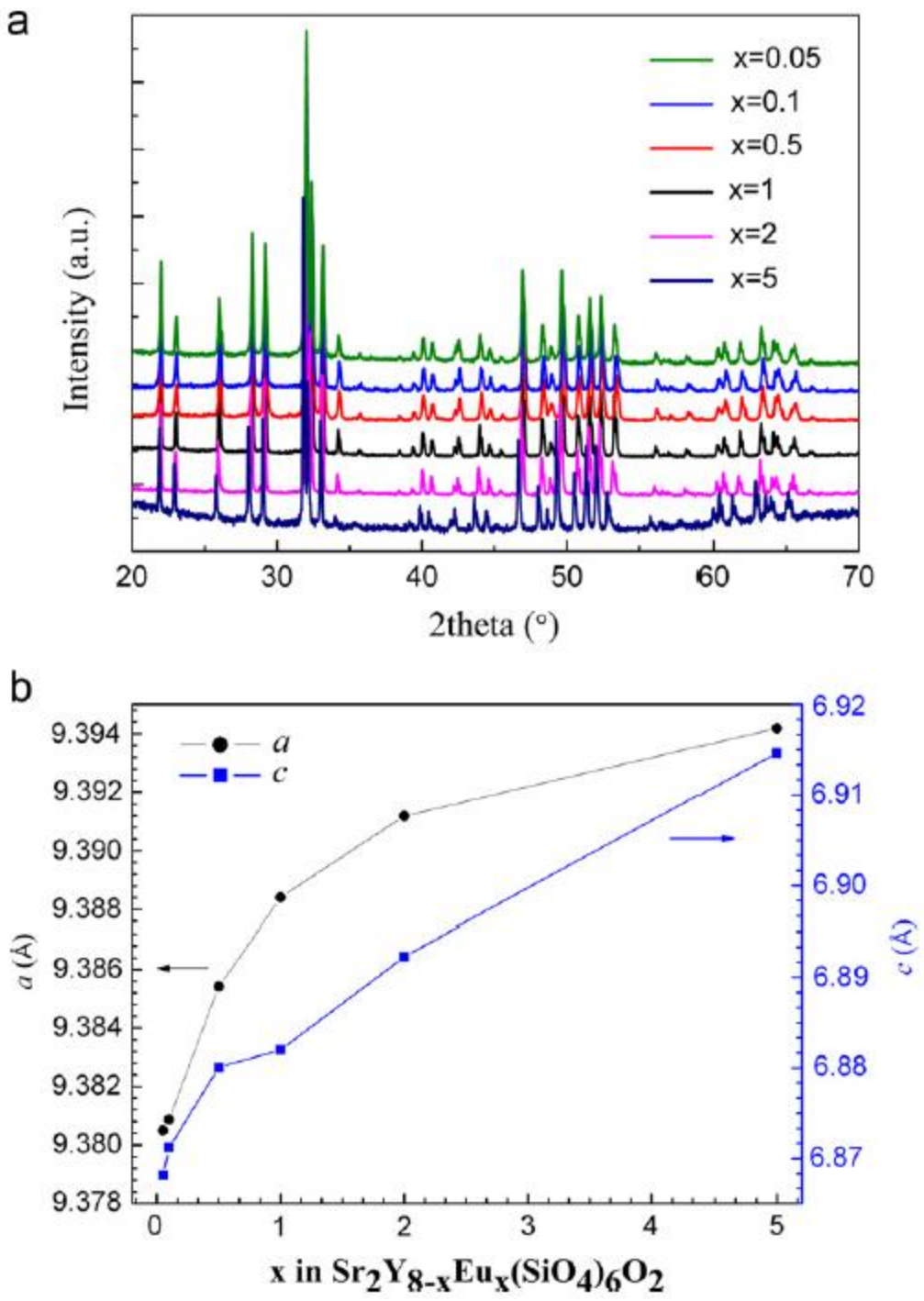
a
x=0.05
x=0.1
x=0.5
x=1
x=2
x=5
Intensity (a.u.)
20
30
40
50
60
70
2theta (°)
b
a
c
9.394
9.392
9.390
9.388
9.386
9.384
9.382
9.380
9.378
a (Å)
6.92
6.91
6.90
6.89
6.88
6.87
c (Å)
0
1
2
3
4
5
x in Sr2Y8-xEux(SiO4)6O2

Fig. 2

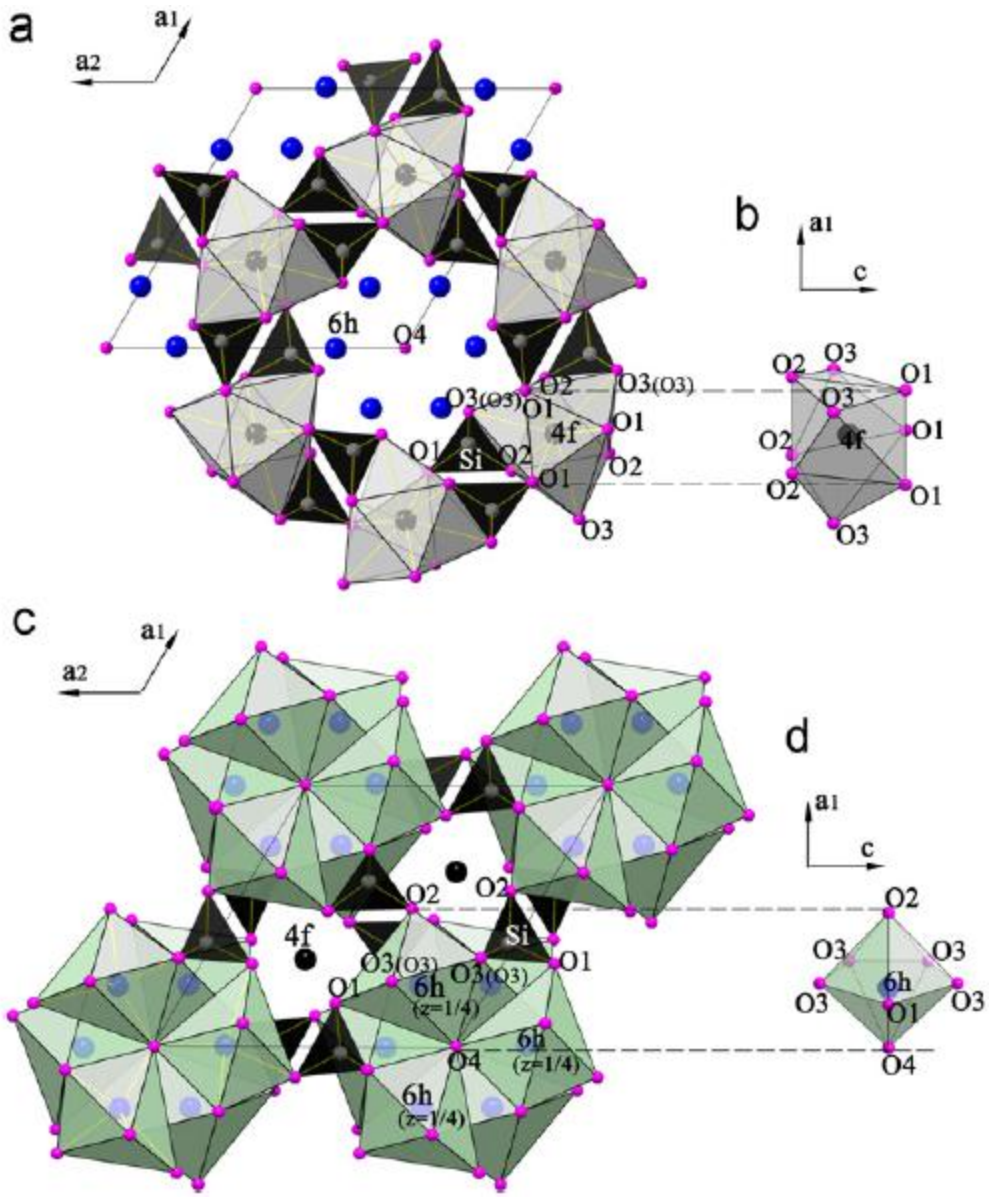
a
a1
a2
6h
O4
O3(O3)
O2
O1
4f
Si
O3
b
a1
c
O2
O3
O1
4f
c
a1
a2
O2
Si
4f
O3(O3)
O1
6h
(z=1/4)
O4
d
a1
c
O2
O3
6h
O1
O4

Fig. 3

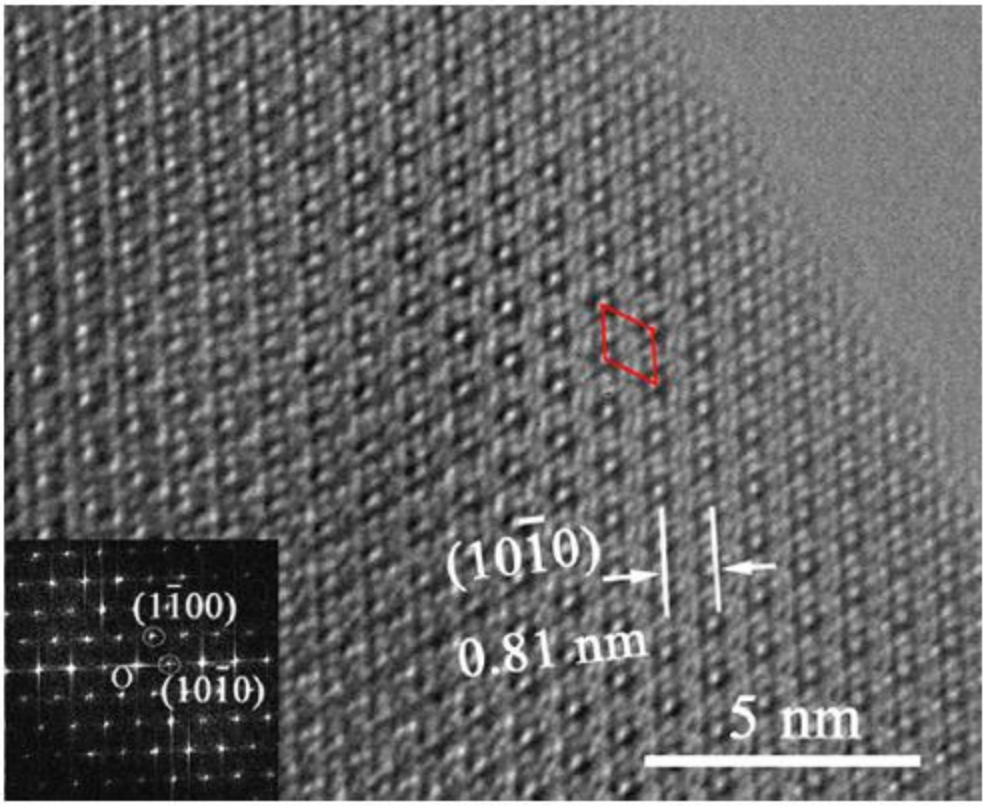

Fig. 4

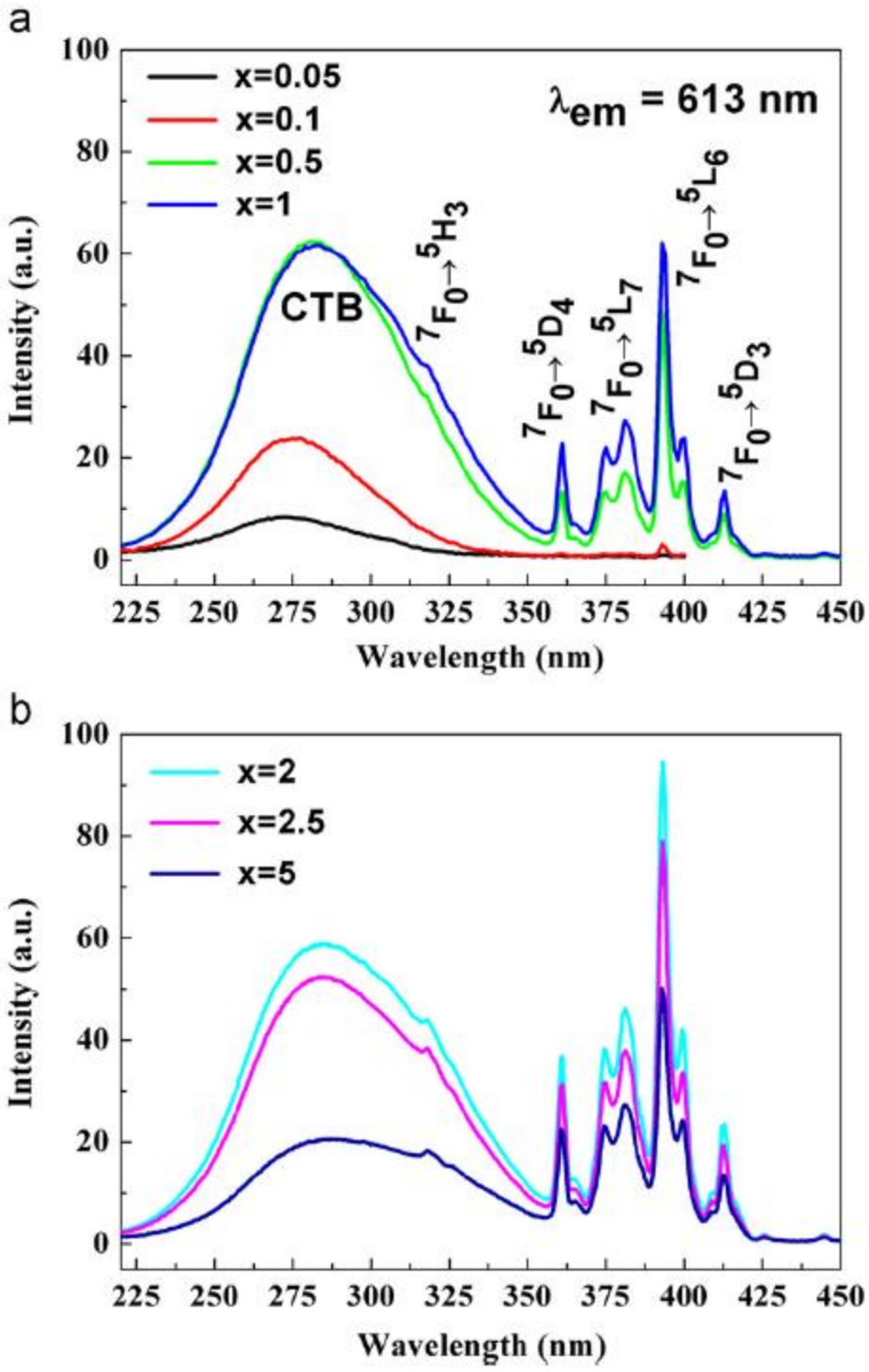
a
x=0.05
x=0.1
x=0.5
x=1
λem = 613 nm
CTB
7F0→5H3
7F0→5D4
7F0→5L7
7F0→5L6
7F0→5D3
Intensity (a.u.)
Wavelength (nm)
b
x=2
x=2.5
x=5
Intensity (a.u.)
Wavelength (nm)

Fig. 5

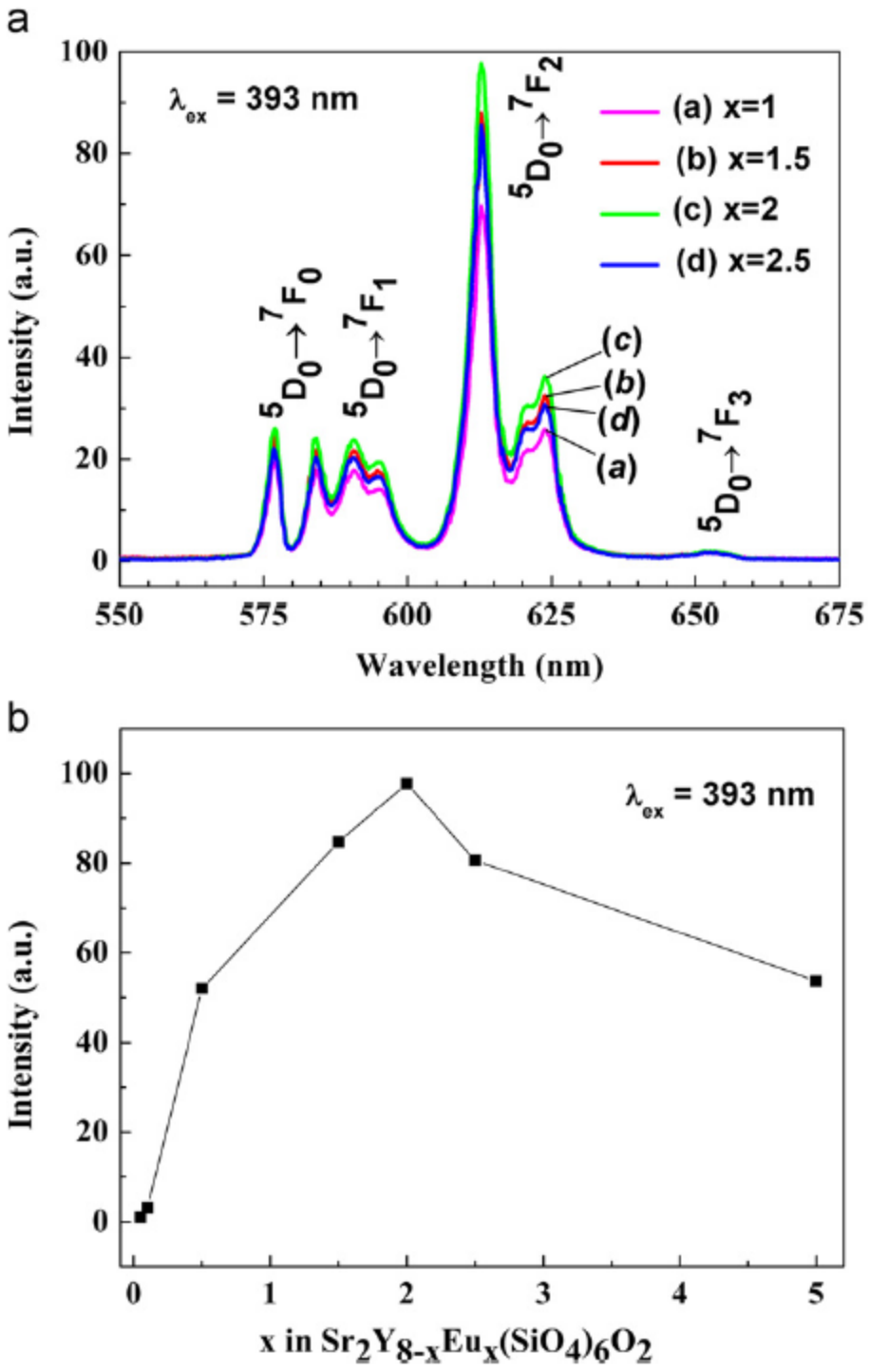
a
λex = 393 nm
(a) x=1
(b) x=1.5
(c) x=2
(d) x=2.5
5D0→7F0
5D0→7F1
5D0→7F2
5D0→7F3
(c)
(b)
(d)
(a)
Intensity (a.u.)
Wavelength (nm)
b
λex = 393 nm
Intensity (a.u.)
x in Sr2Y8-xEux(SiO4)6O2

Fig. 6

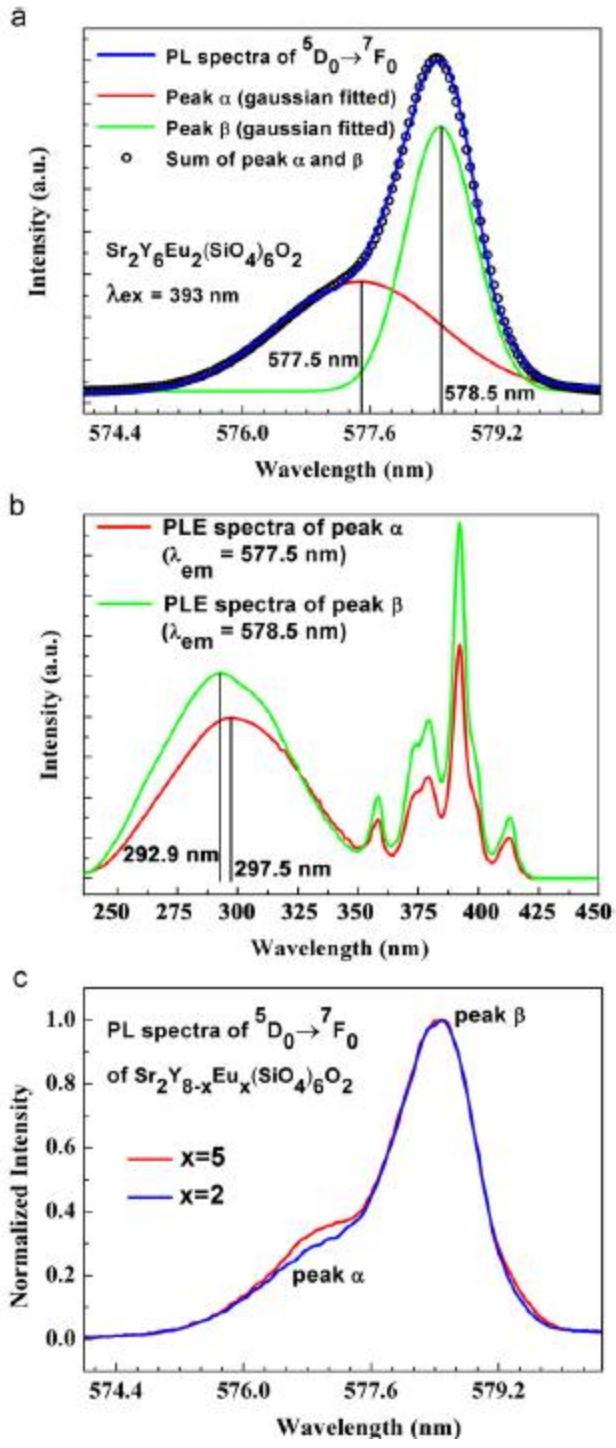
a
PL spectra of $^5D_0 \rightarrow {}^7F_0$
Peak α (gaussian fitted)
Peak β (gaussian fitted)
Sum of peak α and β
$Sr_2Y_6Eu_2(SiO_4)_6O_2$
λex = 393 nm
577.5 nm
578.5 nm
Intensity (a.u.)
574.4
576.0
577.6
579.2
Wavelength (nm)
b
PLE spectra of peak α
(λ_{em} = 577.5 nm)
PLE spectra of peak β
(λ_{em} = 578.5 nm)
292.9 nm
297.5 nm
Intensity (a.u.)
250 275 300 325 350 375 400 425 450
Wavelength (nm)
c
PL spectra of $^5D_0 \rightarrow {}^7F_0$
of $Sr_2Y_{8-x}Eu_x(SiO_4)_6O_2$
x=5
x=2
peak β
peak α
Normalized Intensity
1.0
0.8
0.6
0.4
0.2
0.0
574.4
576.0
577.6
579.2
Wavelength (nm)

Fig. 7